



**HAL**  
open science

## Crustal structure deduced from receiver functions via single-scattering migration

E. Bertrand, Anne Deschamps, J. Virieux

► **To cite this version:**

E. Bertrand, Anne Deschamps, J. Virieux. Crustal structure deduced from receiver functions via single-scattering migration. *Geophysical Journal International*, 2002, 150 (2), pp.524-541 [416]. 10.1046/j.1365-246X.2002.01723.x . hal-00406659

**HAL Id: hal-00406659**

**<https://hal.science/hal-00406659>**

Submitted on 27 Jan 2021

**HAL** is a multi-disciplinary open access archive for the deposit and dissemination of scientific research documents, whether they are published or not. The documents may come from teaching and research institutions in France or abroad, or from public or private research centers.

L'archive ouverte pluridisciplinaire **HAL**, est destinée au dépôt et à la diffusion de documents scientifiques de niveau recherche, publiés ou non, émanant des établissements d'enseignement et de recherche français ou étrangers, des laboratoires publics ou privés.

# Crustal structure deduced from receiver functions via single-scattering migration

E. Bertrand,\* A. Deschamps and J. Virieux

Géosciences Azur, UMR 6526 CNRS-UNSA-UPMC-IRD, 250 rue A. Einstein, 06560 Sophia Antipolis, France. E-mail: deschamps@geoazur.unice.fr

Accepted 2002 March 13. Received 2002 February 19; in original form 2000 December 19

## SUMMARY

An investigation of the teleseismic *P*-wave coda is performed using the single-scattering approximation. The method allows one to image short-wavelength scale ( $\leq 2$  km) velocity and density heterogeneities and structures that are barely detected by traveltimes tomography. Source effects are removed by using receiver functions for data interpretation, but the amplitude (especially the sign of the signal) is synthesized. Both broad-band seismological stations in the southwestern Alps (France) and Campanian plain (Italy) are used for the illustration of the proposed method. Because of the large aperture of our arrays, laterally small-scale heterogeneities are difficult to image and we must assume lateral continuity of the detectable structure. If so, we show that this depth migration based on a single-scattering approach can recover both the depth and the geometry of the main discontinuities below the studied areas. In the southwestern Alps, we underline a complex crustal structure and Moho dipping topography. The Moho depth increases from 20 to 30 km between the coastline and the Mercantour range. In the Campanian plain (surrounding Mount Vesuvius) we also find a southeastwards-dipping Moho. Furthermore, the three main discontinuities are imaged, showing a relatively shallow mantle–crust discontinuity and a deeper one near the coastline.

**Key words:** body waves, broad-band, crustal structure, Moho discontinuity, *P*-to-*S* conversions, scattering, waveform analysis.

## 1 INTRODUCTION

Since the late 1970s, many experiments have been performed in order to recover the depth of crust and mantle discontinuities by analysing the teleseismic *P*-coda (e.g. Burdick & Langston 1977; Langston 1977; Vinnik 1977). Most of these studies consider a near vertically propagating plane *P* wave generating a converted *S* wave when passing through sharp horizontal discontinuities. The *P*-converted *S* phase is typically of low amplitude; this signal is then enhanced by computing receiver functions. These functions are obtained by deconvolution of the horizontal components by the vertical one and can be considered as source-normalized horizontal-component seismograms (Ammon *et al.* 1990; Bertrand 2000; Bertrand & Deschamps 2000).

Synthetic seismograms generated for plane-layered structures show dominant *P*–*S*-converted phases on the radial-component and zero amplitude on the transverse component (Abers 1998; Cassidy 1992). Nevertheless, real data often show high amplitude on the transverse component that is mainly explained by anisotropic media or dipping discontinuities (Langston 1979; Abers 1998; Jones & Phinney 1998; Girardin & Farra 1998).

In some recent studies, high-frequency signals generated by near-receiver scattering in teleseismic *P*-coda have been investigated (i.e. Abers 1998). These experiments are based on broad-band recordings at small aperture arrays installed in tectonically complicated areas.

In order to identify the source of the scattered energy, one can assume single *P*-to-*S* scattering and *back-propagate* the set of data into a 3-D volume (Revenaugh 1995; Abers 1998; Bostock 1999). This rather simple procedure also allows the imaging of discontinuities. In this paper we explain the inversion scheme and give some synthetic examples. We apply this procedure to data recorded in the southern French Alps by the TGRS network and by a temporary array in the Campanian region (southern Italy).

Because the studied area in southeastern France is bordered by the Ligurian basin (Mediterranean sea) to the south and by the Mercantour range to the north, the structure beneath the area is expected to be complicated. Indeed, previous studies (e.g. Bethoux *et al.* 1986; Blundell *et al.* 1992; Calais *et al.* 1993; Fontaine 1996) show a very thin continental crust under the Ligurian sea margin and a 35 km deep crustal root under the southern Alps. Furthermore, the ongoing convergence between Africa and Europe creates shortening structures in both the Alpine continental crust and the Ligurian oceanic crust (Bethoux *et al.* 1992; Augliera *et al.* 1994; Fontaine 1996; Laurent 1998). Shortening affects the whole crust and generates strong lateral heterogeneity.

\*Now at: BRGM, 117 av. de Luminy, 13276 Marseille Cedex 9, France.

For the Campanian plain, the strong lateral heterogeneity in the crust may be related to crustal thinning of the Tyrrhenian basin and to volcanic complexes such as Mount Vesuvius (Scarascia *et al.* 1994).

## 2 DATA ANALYSIS

Previous studies (e.g. Langston 1979; Vinnik *et al.* 1983; Ammon 1991) have shown that the coda of the teleseismic *P* wave can be interpreted in terms of reflections and transmissions of mode-converted waves at discrete boundaries beneath a seismological station. By the deconvolution of the vertical component from the horizontal ones, we compute receiver functions removing source effects and isolate the converted waves. Because of the nearly vertical incidence of *P* waves, the receiver function method shows accurate vertical resolution.

From the worldwide earthquake catalogue edited by the CNSS (Council of the National Seismic System), we select events recorded simultaneously at all the stations of the considered array. We take care of the magnitude and the epicentral distance and eliminate all the earthquakes occurring at a distance of less than 30° or more than 90° from the array. Events with a body-wave magnitude of less than 5.7 are rarely useful for the computation of receiver function unless they occur at distances less than 50° from the recording site. Because of the geographical distribution of earthquakes, we mainly record events of epicentral distance larger than 60° and thus we select events with magnitude larger than 6.0.

Receiver functions are obtained from the broad-band seismograms using a time-domain deconvolution of the horizontal components (radial and transverse) by the vertical one. In this procedure, an equal length of signal is considered for all components.

The convolutional relationship between the vertical and radial (or transverse) components is regarded as an invertible system of time equations. This system is then solved using a singular-value decomposition. The complete description of the receiver computation procedure is given in previous publications (Bertrand 2000; Bertrand & Deschamps 2000).

### 2.1 Southern French Alps

In the Southern French Alps, north of the French Riviera, three broad-band stations CALF, STET, SAOF from the TGRS network can be used as an array with an aperture of about 50 km (Fig. 1). The stations were set up progressively between 1994 and 1996; this time window allows the computation of 33 receiver functions from teleseismic events. The time signals from Strekeisen STS-2 sensors are recorded at 125 Hz for recognized events and at 1 Hz continuously by a Titan (Agecodagis) acquisition system.

For each station, we consider both radial and transverse receiver functions. The functions obtained are plotted with respect to the associated theoretical *P*-wave backazimuth (Figs 2–4). Converted phases can be easily tracked at the CALF station (Fig. 2) with a clear pattern depending on the *P*-wave backazimuth: energy arriving from the north shows a coherent pattern. There is non-negligible energy on the transverse component, especially from the west. The receiver functions at the station SAOF show a different pattern with less coherence on converted phases and less energy on the transverse component. The station STET signature is similar to CALF on the radial component while the transverse component displays strong energy coming from events to the south and the east. This azimuthal dependence has been reported and interpreted as related to the Moho topography beneath the Southern French Alps (Bertrand & Deschamps 2000).

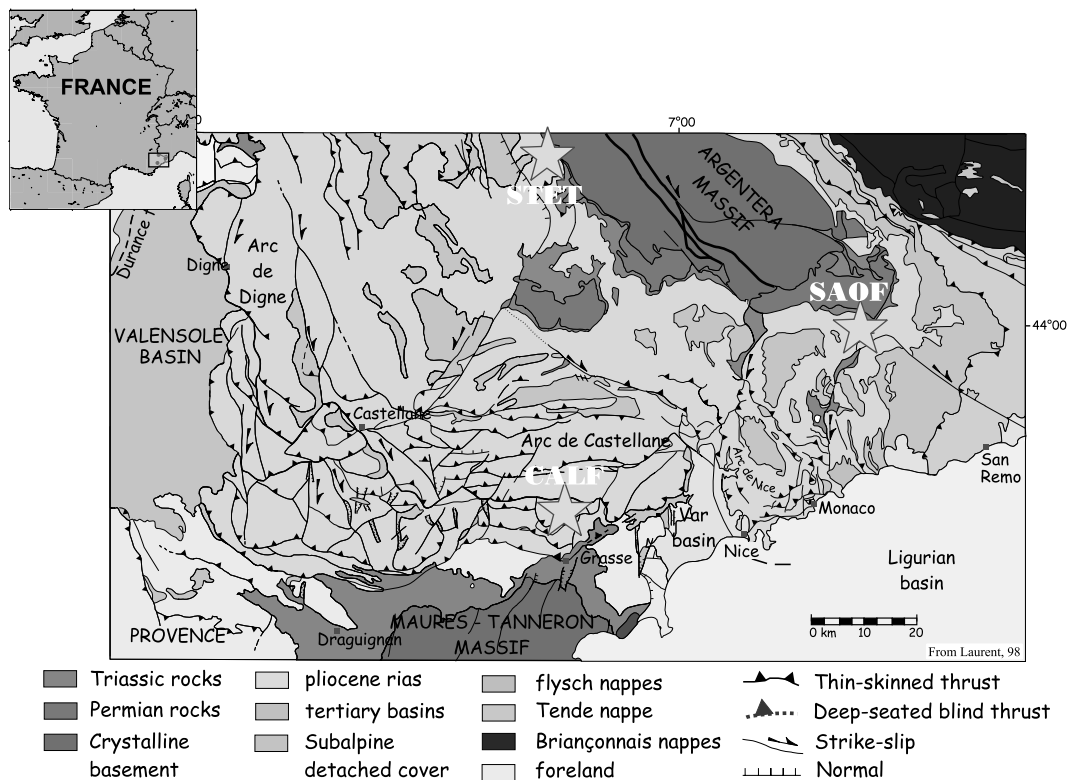


**Figure 1.** Tectonical setting of the TGRS network in the French Maritime Alps. In this region the network is composed of three stations: CALF, STET and SAOF. The structural map is after Laurent (1998).

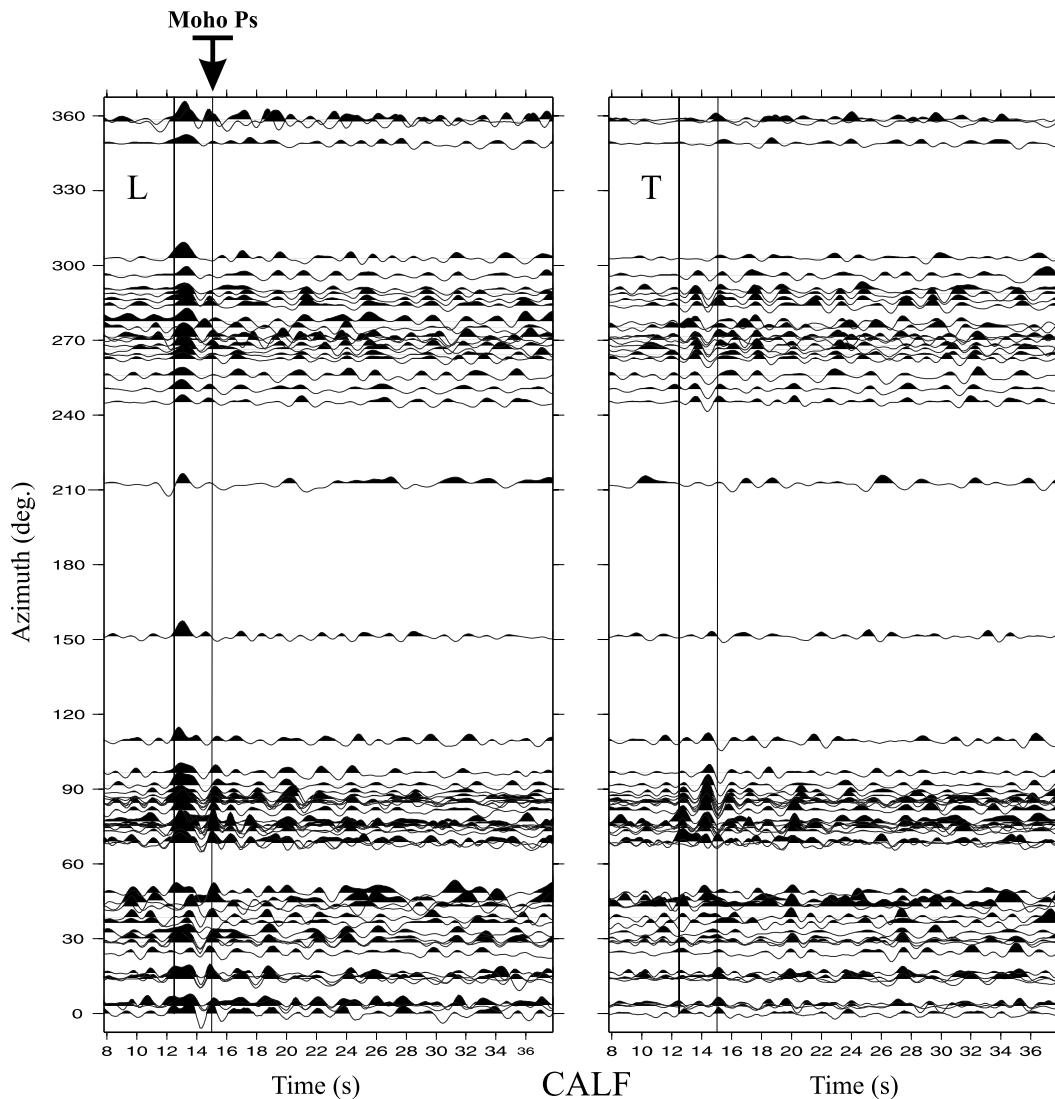


**Figure 2.** Receiver functions computed at station CALF plotted with respect to the associated backazimuth. All traces are plotted with the same amplitude scale and aligned in time. The first vertical line shows the  $P$  wave, the second one the  $P$ -to- $S$  converted phase at the Moho. L: longitudinal component, T: transverse component.

## 2.2 Campanian plain

The Vesuvius volcano (Naples, Italy) is situated in the Miocene tectonic graben of the Campanian plain. This graben is filled with alluvial sediments and volcanic rocks and is embedded in Mesozoic carbonate platforms that subsided during the Pliocene and Pleistocene with a maximum vertical extent of 5 km (Scandone *et al.* 1991; Zollo *et al.* 1996). The graben origin has been related to a stretching and thinning of the continental crust by the counterclockwise rotation of the Italian peninsula and the contemporaneous opening of the Tyrrhenian sea with the consequent subsidence of the carbonate platform along most of the Tyrrhenian coast (Scandone *et al.* 1991). Voluminous volcanic activity of Campi Flegrei, Vesuvius and the island of Procida occurred along the coast of this plain during the last 50 000 yr. The limestone outcrops 10–15 km southeast of the volcano (Fig. 5).

Within the framework of the BROADVES project (1997–2000), a French–Italian broad-band seismological experiment, we deployed digital three-component seismic stations around the Vesuvius vol-

cano (Fig. 5). In this paper, we mainly use recordings at four of them: CAP on Capri island, southwest of Vesuvius, FAI, TOR and CIC to the east and north of Vesuvius. FAI is the closest station to the volcano at a distance of 15 km. The stations are at a distance of about 25 km from each other and are all installed on limestone rock. They are composed of Guralp CMG40 and CMG3 sensors connected to Reftek 24 bit digital acquisition systems. The ground motion has been recorded simultaneously at each station with a sampling rate of 50 Hz.

We recorded the worldwide natural seismicity continuously over 5 months and 23 events were used to compute receiver functions. Their distribution is presented in Fig. 6. Most of events occur at a distance larger than  $80^\circ$  from the studied area. The backazimuths are in the range  $N5^\circ$ – $85^\circ$ .

During the experiment, seven earthquakes with a magnitude larger than 6.0 occurred in the Aleutian island (southwest Alaska)  $87^\circ$  away from the Campanian plain. The backazimuth associated with these events is close to  $N10^\circ$ . We plot in Fig. 7 the receiver functions obtained with the seismograms recorded at station TOR,

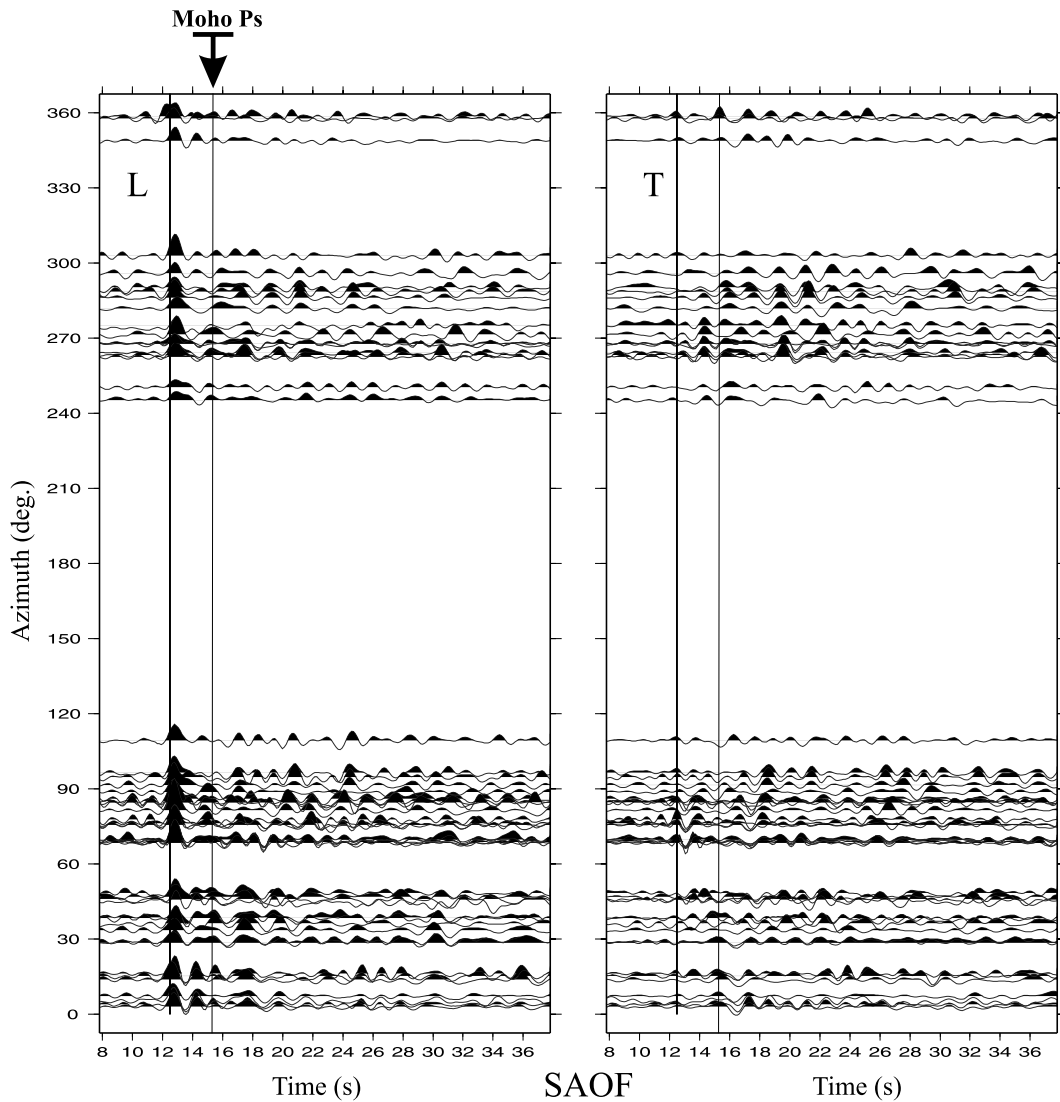


Figure 3. Receiver functions computed at SAOF station. Same plotting criteria as Fig. 2.

CIC and FAI. We compute the transverse receiver functions as well as the radial one. The seven functions are similar for a given station but the observed waveforms vary from one station to another. All receiver functions show a significant amount of energy in the transverse component. This set of data provides us with several observations. As for a given station where we obtained similar receiver functions from different events occurring in the same area, we show that the technique properly removes the earthquake source wavelet from the recorded body wave. Secondly, the waveform differences observed between the recordings of the three stations underline the complexity of the crustal structure beneath the array. The high heterogeneity in the crust results in an appreciable incoherence of the recorded  $P$ -coda at each station of the seismic broad-band array.

### 3 SCATTERER LOCATION: METHOD

The receiver functions computed for both the Southern French Alps and for the Campanian plain show an important transverse component signal that cannot be explained with a simple plane layered crustal structure. In order to test whether near-receiver scattering

could be the source of the transverse ground motion pointed out at the arrays, we propose to apply an inversion procedure somewhat similar to the previous inversions of  $P$ -coda (Lynnes & Lay 1989; Revenaugh 1995); however, rather than inverting only the radial receiver function (Abers 1998) we consider both the radial and the transverse components of the ground motion. Indeed, we consider the total horizontal energy of the  $P$ -coda by inverting the function

$$F(t) = \sqrt{L^2(t) + T^2(t)}, \quad (1)$$

where  $L(t)$  and  $T(t)$  are the radial (or longitudinal) and transverse receiver functions, respectively. The method described below assumes single  $P$ -to- $S$  scattering because the receiver functions are assumed to be mainly composed of  $S$ -mode-converted waves.

Following Abers (1998), we consider a homogenous medium beneath the array described by a uniform grid (Fig. 8). Each grid node is tested as a potential scatterer and the method stacks records to compute the power owing to scatterers at that location. At each node and for each station, we compute the delay between the direct  $P$  wave and the single-scattered  $P$ -to- $S$  conversion. A constant  $P$  and  $S$  velocity is assumed in order to simplify the computation effort in this attempt. We consider velocities of 6.4 and 3.7 km s<sup>-1</sup> for  $P$  and

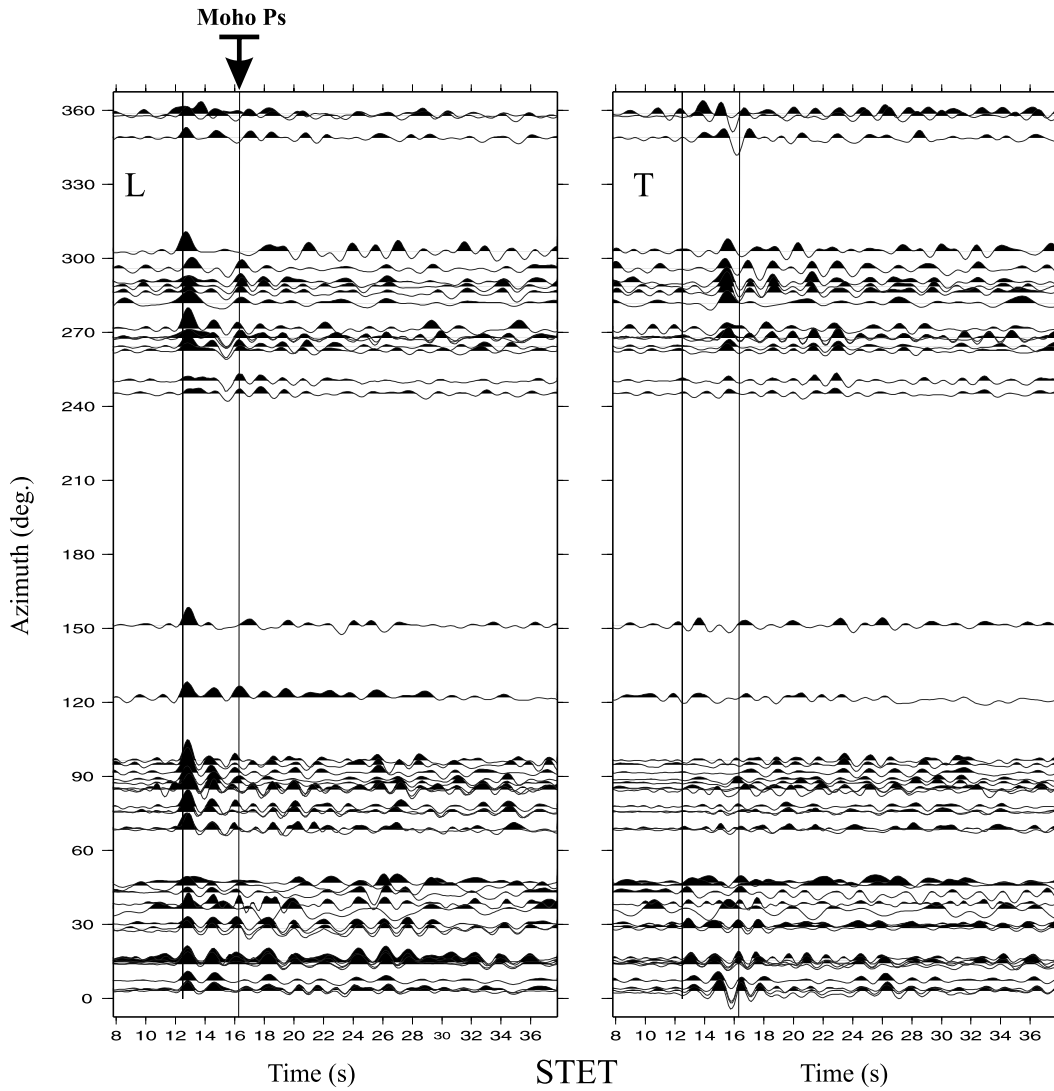


Figure 4. Receiver functions computed at STET station. Same plotting criteria as Fig. 2.

*S* waves, respectively, as suggested by Abers (1998) for the typical average velocity values in the continental crust. Finally, we suppose that the incident energy travels as a plane *P* wave before scattering, which is correct for teleseismic events. For a given *P* wave a set of delays are computed for each grid node. The corresponding amplitudes taken on the receiver function are then stacked and the value is assigned as the scattering power for the corresponding node. For a set of receiver functions and stations we have

$$S(x, y, z) = \sum_{j=1}^n \sum_{r=1}^m F_{i,r}[\Delta t(x, y, z)], \quad (2)$$

where  $F_{i,r}$  is the  $i$ th receiver function computed at the  $r$ th seismic station and  $(x, y, z)$  are the coordinates of the considered node. The delay between the direct *P* wave and the scattered wave,  $\Delta t$ , is a function of the considered node coordinates but also depends on the *P*-wave azimuth and the angle of incidence (Fig. 8). At this stage we do not consider any weighting factor to match the scattering radiation pattern (Forgues & Lambaré 1997). Thus, for simplicity, we consider isotropic scattering, which provides the same amplitude at each grid node with the same delay time.

### 3.1 Single-scattered *P*-to-*S* isochrone

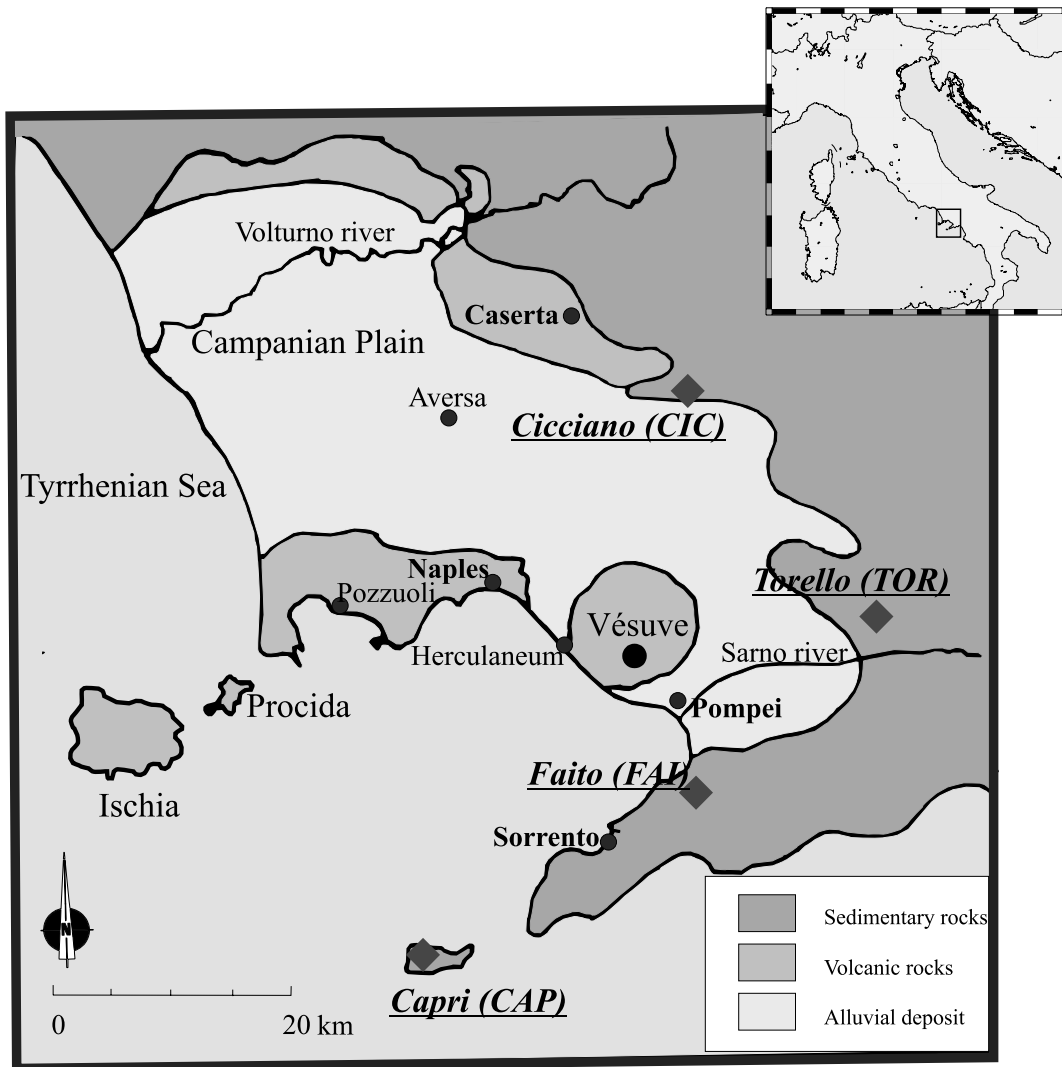
In 2-D, an isochrone is a curve including scatterers that generate *S* waves recorded simultaneously at the seismic station. Considering a vertically propagating plane *P* wave (Fig. 8) and a station at the origin of the coordinates, the isochrone corresponding to the arrival time  $t = T_p + \Delta t$  can be expressed as

$$\frac{D + y}{\alpha} + \frac{\sqrt{x^2 + y^2}}{\beta} = \frac{D}{\beta}, \quad \text{where } D = \frac{\Delta t}{\beta^{-1} - \alpha^{-1}}. \quad (3)$$

In this equation,  $\alpha$  and  $\beta$  are the *P* and *S* velocities, respectively, and  $(x, y)$  are the coordinates of the diffractor. The expression (3) becomes

$$x^2 = y^2(Rv^{-2} - 1) + 2yDRv^{-1}(Rv^{-1} - 1) + D^2(1 - Rv^{-1})^2. \quad (4)$$

where  $Rv$  is the velocity ratio between the *P* and *S* propagation ( $Rv = \alpha/\beta$ ). The isochron is then an ellipse with its main axis parallel to the incoming *P*-wave direction of travel and one of its foci at the recording point.



◆ BROADVES seismic stations

Figure 5. Temporary broad-band array used in the Campanian plain (southern Italy). Three stations (CAP, FAI, TOR) form a SW–NE seismic profile.

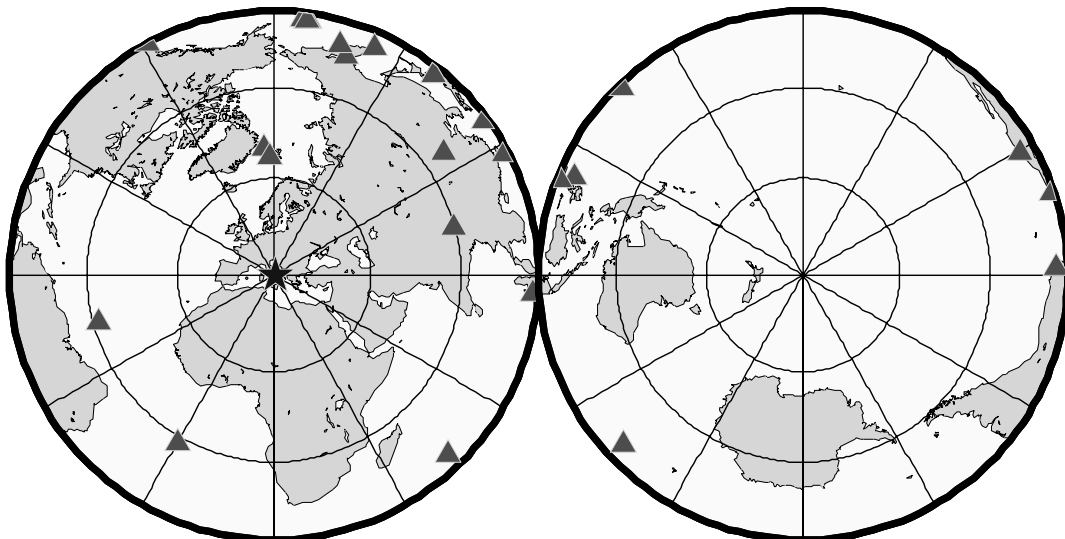
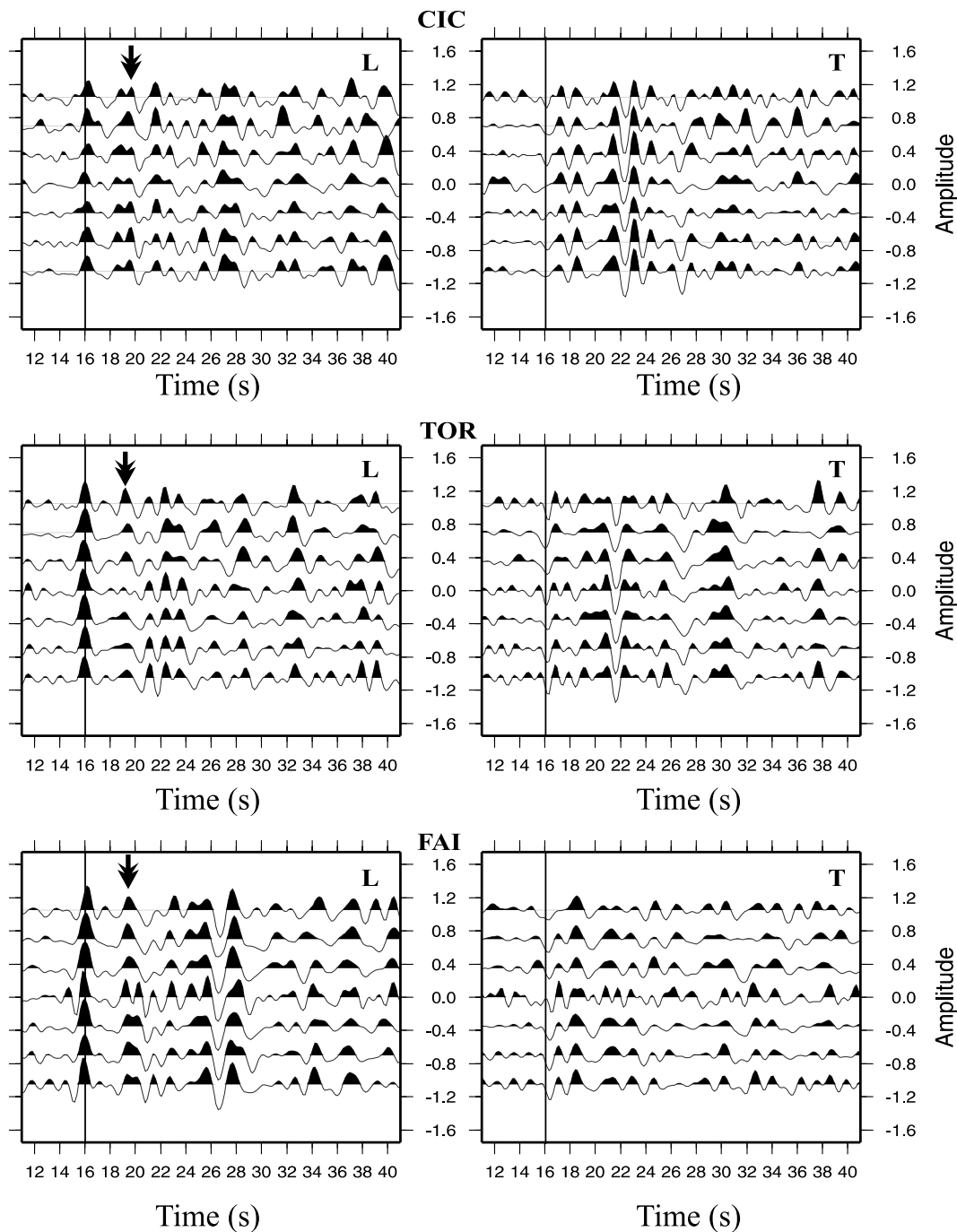


Figure 6. Teleseismic events recorded at the BROADVES array and used to compute the receiver functions.



**Figure 7.** Receiver functions derived from Aleutian earthquakes recorded at the BROADVES stations. The backazimuth of all events is close to  $N10^\circ$ . L: longitudinal component, T: transverse component. The amplitude scale is the same for all traces. Traces are aligned at the same  $P$  arrival time (vertical line). The double arrow shows  $P$ -to- $S$  converted phase at the Moho.

In order to test our method we invert a simple synthetic signal composed of a single diffracted  $PS$  phase emerging 3.34 s after the main peak of the receiver function (Fig. 9). The  $P$  incidence angle is assumed to be  $20^\circ$ . The power grid corresponding to this synthetic signal clearly shows the ellipse associated with the scattering energy observed for the receiver function (Fig. 9). Owing to the width of the main peak of the function, some power corresponding to a  $P$ -to- $S$  interpretation of the  $P$ -signal is detected directly beneath the recording point. The power map accurately matches the shape of the theoretical isochrone as given by eq. (4).

With only one single-receiver function it is not possible to recover the position of the scatterer. By stacking a number of receiver functions we should focus the scatterer location on the power grid beneath even a single station, although the sampling has a narrow aperture. However, the use of arrays allows us to seek more precisely for scatterer locations. In order to illustrate this point we compute synthetic signals for a homogeneous medium with one diffractor beneath an array composed of three stations (Fig. 10). The source of scattered energy is located at the centre of the array, 10 km beneath the surface. Stations are included in a 11.2 km side isosceles

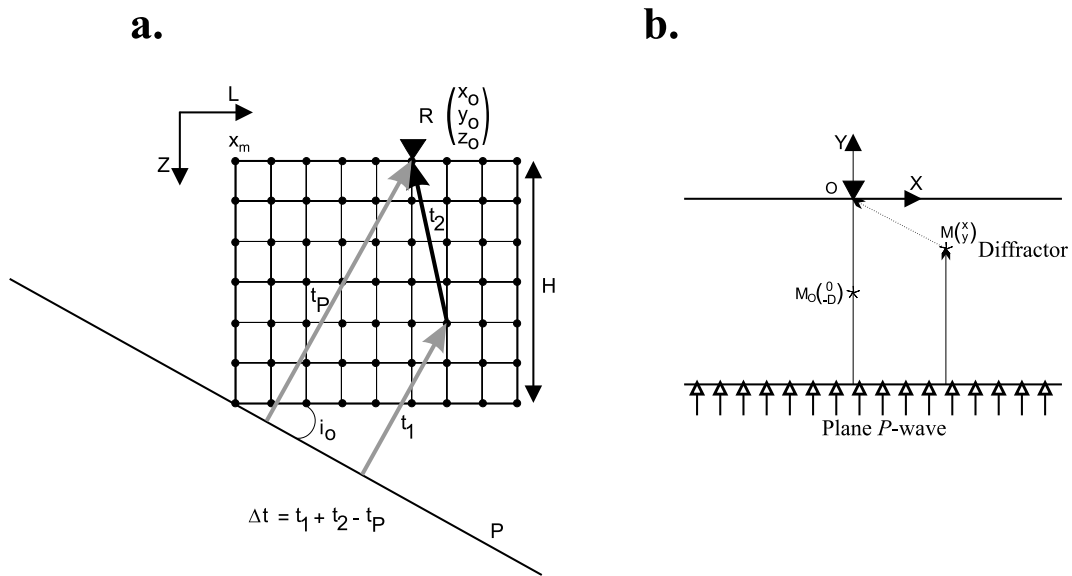


**Figure 8.** (a) Propagation and scattering of a plane  $P$  wave in a gridded homogeneous and isotropic medium. The time delay between the direct  $P$  arrival and the  $PS$  scattered one,  $\Delta t$ , is function of the grid node position, the receiver position and the  $P$  incidence angle. (b) Notation used for eq. (4).

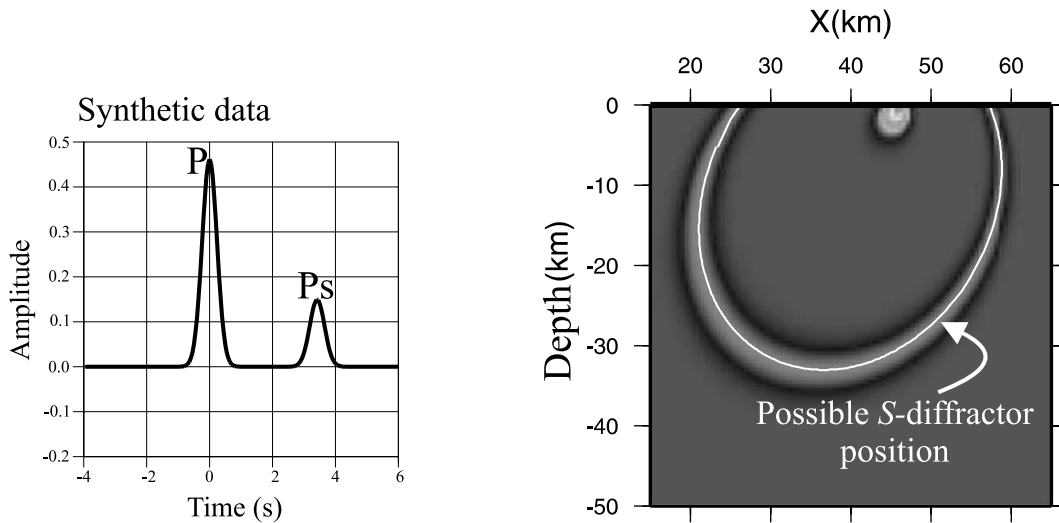


**Figure 9.** Simple synthetic case illustrating the method. One single function (left) is used to computed the power grid. The inverted trace is composed by a main peak and 1 s arrival with a delay close to 3.4 s. A vertical cross-section through the power grid is presented on the right. The section is made in the direction of the  $P$  arrival. The  $P$ -velocity is fixed at  $6.4 \text{ km s}^{-1}$  and we consider a  $3.7 \text{ km s}^{-1}$  velocity for the  $S$  wave. The incidence of the  $P$  wave at the station is  $20^\circ$ .

triangle. By ray tracing, we compute 24 synthetical receiver functions at each station. The radial component is presented in Fig. 10. We exaggerate the amplitude of the scattered wave by a factor of 2. The radiation pattern that describes how a model perturbation component diffracts the incoming wave (Forgues & Lambaré 1997) is taken into account in this forward problem. For a single  $PS$  scattering the radiation pattern depends on  $\theta^{PS}$ , the angle between the travel direction of the incident  $P$  wave and that of the generated  $S$  wave,

$$W_{\beta,\alpha,\rho}^{PS} = \left[ -\frac{2\beta}{\alpha} \sin(2\theta^{PS}) \right] \left( \frac{\delta\beta}{\beta} \right) - \left[ \frac{\beta}{\alpha} \sin(2\theta^{PS}) \right] \times \left( \frac{\delta\rho}{\rho} \right) - \frac{\delta\rho}{\rho} \sin\theta^{PS}. \quad (5)$$

$W_{\beta,\alpha,\rho}^{PS}$  represents the ratio of amplitudes of the incoming  $P$  wave and the generated  $S$  wave. At each station, we compute synthetics

for different backazimuths in the range from  $0^\circ$  to  $360^\circ$  and for two different angles of incidence:  $15^\circ$  and  $25^\circ$ . We thus obtain a set of 72 receiver functions (Fig. 10). The amplitude and polarization of the scattered wave,  $PSd$ , are dependent on the backazimuth with a  $2\pi$  period. The polarity change justifies the use of the total horizontal signal (eq. 1) in the inversion rather than the radial receiver function. The  $P$ - $PSd$  delay varies from 1.22 to 1.85 s as a function of backazimuth. From the set of synthetic data we run three grid inversions. The results are shown in Fig. 11. The first inversion (Fig. 11b) is made with only one single-receiver function at each recording point. In a second inversion we test the case of one station with the 24 receiver functions (Fig. 11c) and, finally, the 72 traces are stacked (Fig. 11d). The three power maps are diagonal sections through the grid.

The scatterer location is recovered in each case. However, the use of the 72 receiver functions provides the most precise location,

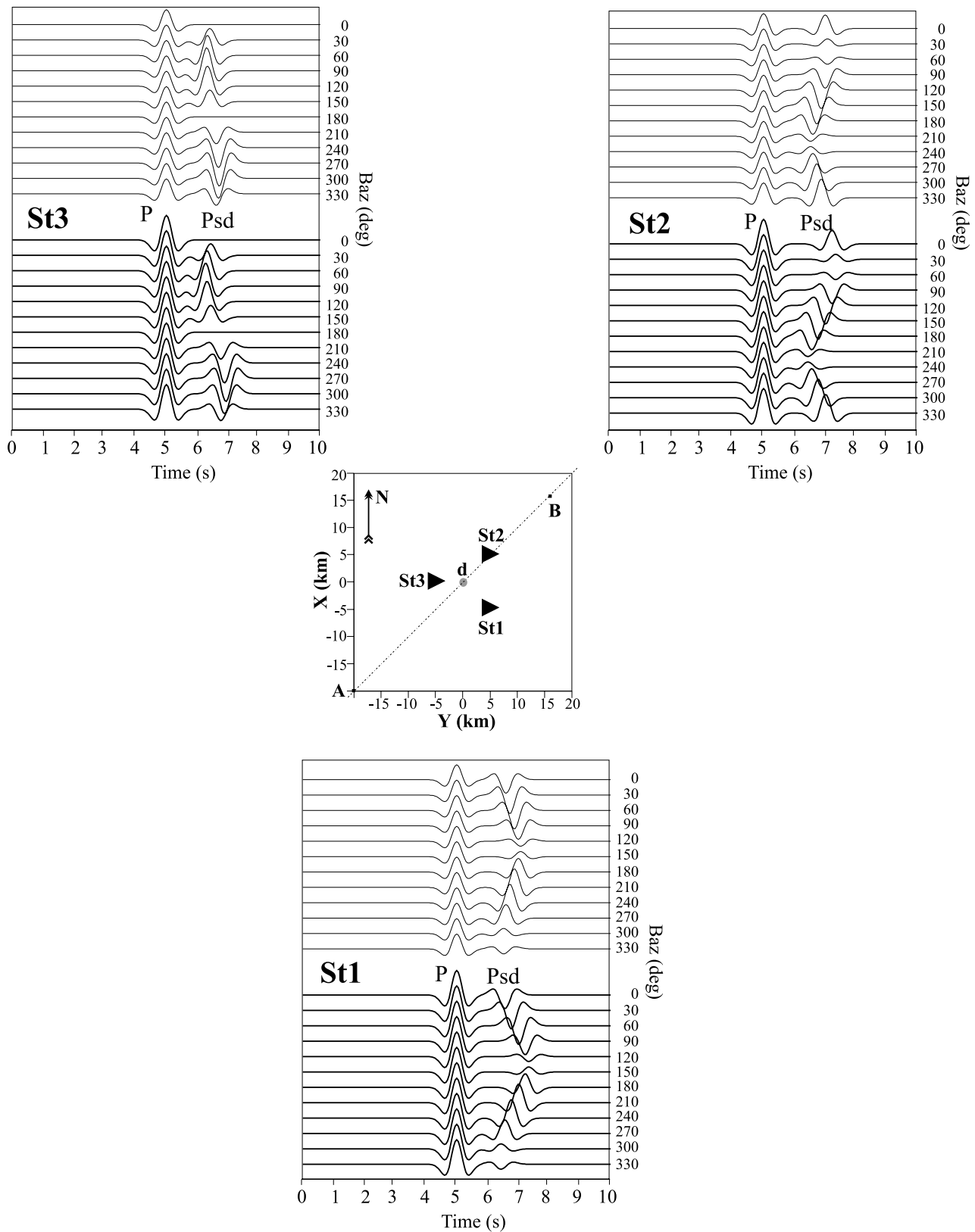


**Figure 10.** Longitudinal component of synthetic seismograms, computed for a plane  $P$  wave propagating in a homogeneous medium in which a diffractor ( $d$ ) is located. Stations define a triangle around the scattering source. At each station, we compute 24 synthetics using different backazimuths and incidence angles. Thick lines are computed considering an incidence of  $25^\circ$ , whereas thin lines are modelled for an incidence angle of  $15^\circ$ . Note that the amplitude and the time arrival of the  $PS$  scattered phase ( $Ps_d$ ) varies like a sinusoid with the backazimuth. The period of variation is  $2\pi$ .

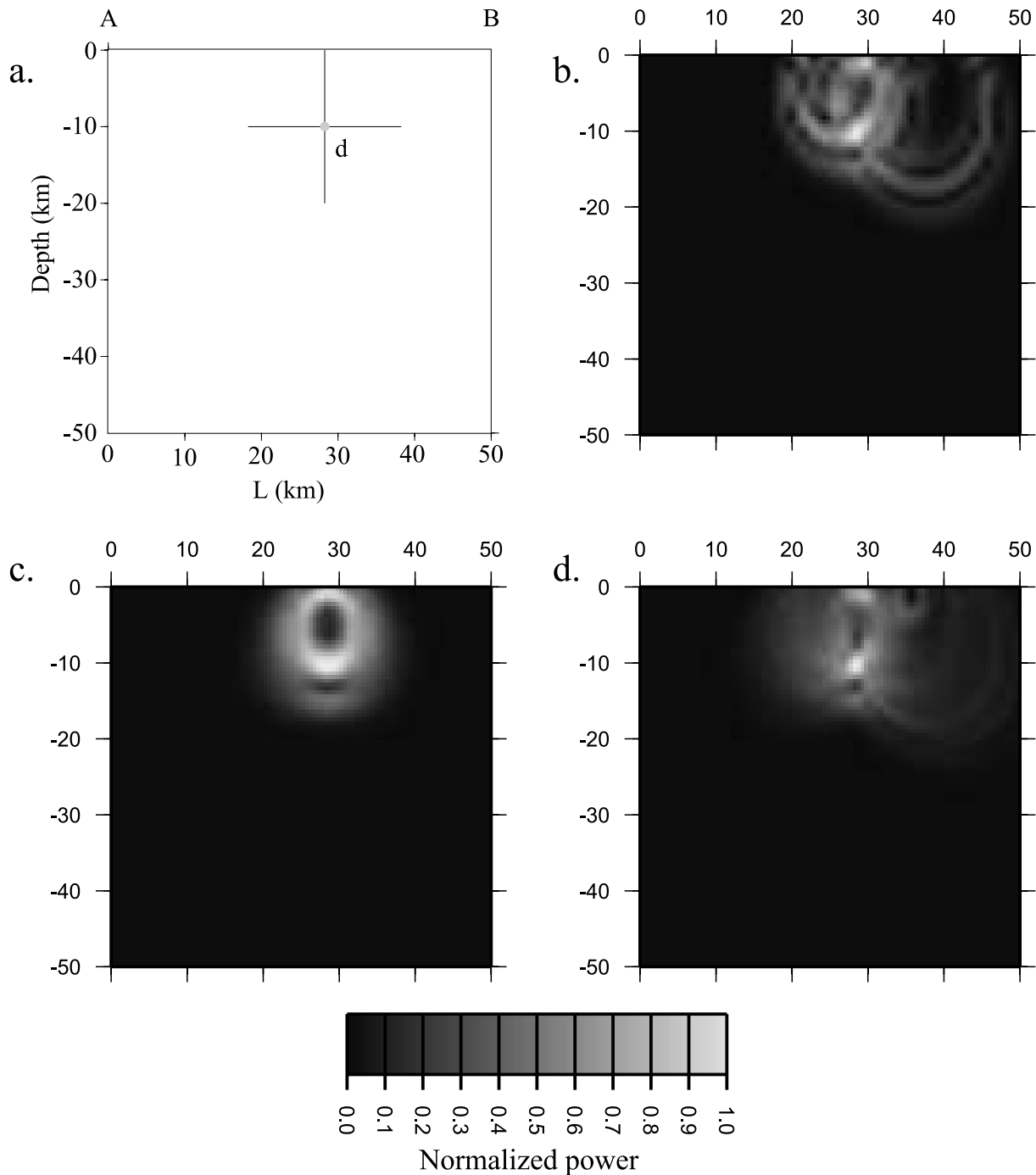


**Figure 11.** Vertical cross-sections along the 50 km length profile (AB), referenced in Fig. 10, in the power grid: (a) position of the diffractor, (b) grid computed with one seismogram at each station (the  $P$  wave is coming from the north), (c) grid computed with 24 seismograms at the station st3, (d) grid computed with all of the synthetics.

whereas the restriction at one single station gives the worst result, although ghost images are still reconstructed.

### 3.2 Plane layer

Previous studies have already shown that the stacking technique we use here is able to recover the  $P$ -to- $S$  conversions at plane discontinuities (e.g. Abers 1998). To test the behaviour of the inversion in the case of a horizontal sharp discontinuity, we compute other

synthetics. This time, the medium beneath a seismic profile is characterized by a 30 km depth discontinuity (Fig. 12). For simplicity, we only synthesize the  $P$ -to- $S$  converted wave. The backazimuth of the incoming  $P$  wave is  $10^\circ$ . Because of the model geometry, the  $P$ - $PS$  delay is the same for all the stations of the profile (3.4 s).

For this simple case the discontinuity already appears on the  $(x, t)$  section. The inversion will result in a migration and we will obtain the  $(x, z)$  section (Fig. 12). In the first section, the discontinuity is relocated at a larger depth than 30 km. Because we are looking for a plane interface we can improve the focusing by the use of a powerful

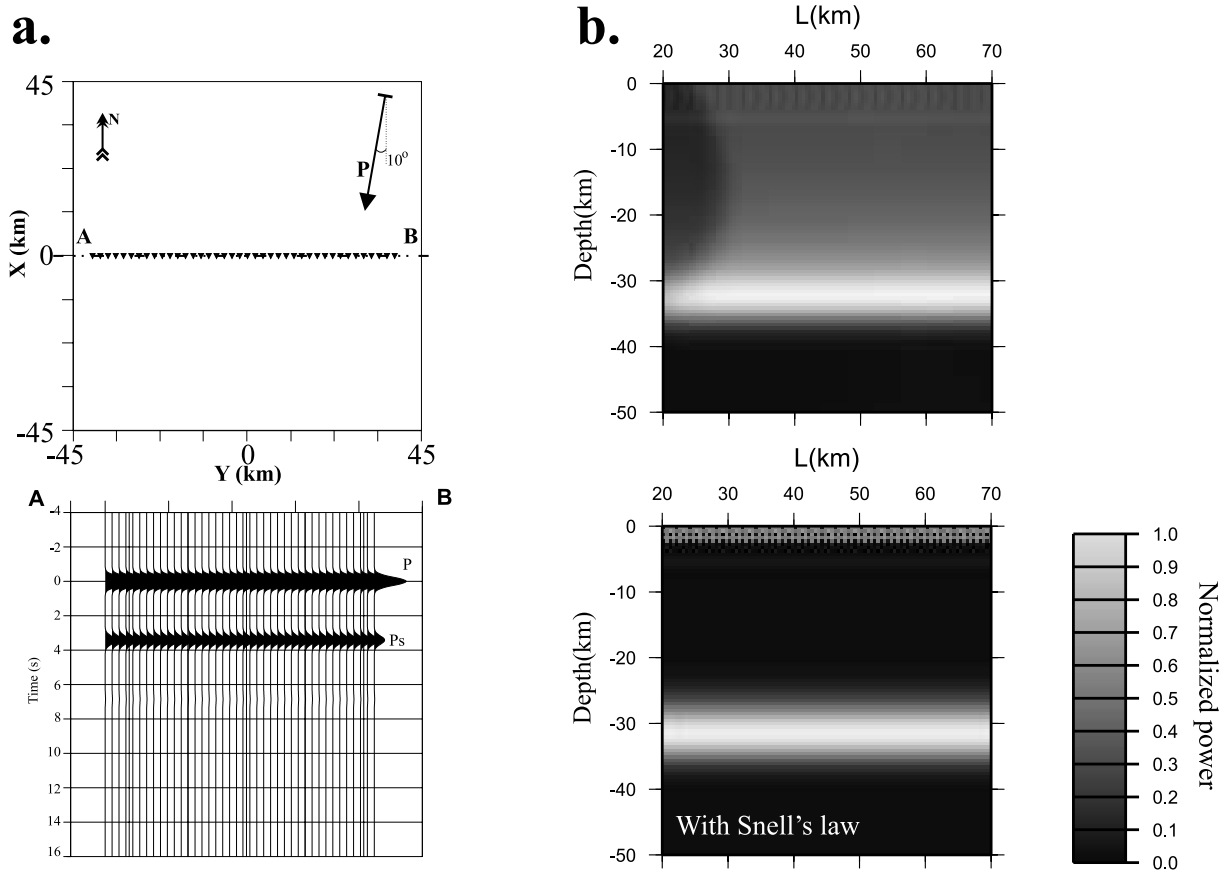


**Figure 12.** (a) Receiver function computed for a medium composed of a homogenous layer located at the top of a half-space. For simplicity, we model only the  $P$ -to- $S$  converted phase on the 30 km depth discontinuity. The acquisition system is a 80 km length E–W-oriented seismic profile. The incoming  $P$  wave is coming from the direction  $N10^\circ$ . (b) East–west vertical cross-section through the diffracting grid. Top: standard inversion which does not assume any interface shape, Bottom: focused inversion using the *a priori* criteria of the Snell's law related to an interface detection.

*a priori* hypothesis: Snell's law which links the incoming  $P$ -wave angle of incidence to the angle of the generated  $S$  wave. We take into account this law by adding to the grid search an appropriate weighting factor

$$S'(x, y, z) = AS(x, y, z) \quad \text{where}$$

$$A = \text{abs} \left[ \cos \left( i_S - \arcsin \left( \frac{\beta_2}{\alpha_1} \sin i_P \right) \right) \right]^n,$$

$$0 \leq A \leq 1, \quad (6)$$

where  $i_S$  is the incidence angle of the considered  $S$  arrival direction,  $i_P$  is the incoming  $P$  wave incidence,  $\alpha$  and  $\beta$  are the  $P$ - and  $S$ -wave velocity, respectively. When the angle  $i_S$  corresponds to the  $S$  wave observed at the station, this angle equals  $\arcsin(\sin i_P \cdot \beta_2/\alpha_1)$  and then the constant  $A$  equals 1. The power  $n$  defines how the search is focused on this point. We choose a value of  $n = 20$  that allows sharp angle discrimination. Thus the response of the scatterer is no longer an ellipse but is focused on a small section of it. The depth of the discontinuity is then well recovered (Fig. 12).

### 3.3 Dipping layer

We test the migration in the case of a dipping discontinuity. Synthetics are generated using 3-D ray tracing (Virieux & Farra 1991) in a simple model composed of a single homogeneous layer over a half-space. The boundary is dipping  $10^\circ$  eastwards (Fig. 13). We

compute receiver functions at 40 stations along an 80 km east–west seismic profile assuming that the incoming wave is a plane  $P$  wave arriving from the half-space underneath the homogeneous layer. The discontinuity beneath the first station west of the profile is at 30 km depth. The  $P$  wave is assumed to propagate from the east (backazimuth of  $90^\circ$ ) and thus waves travel updip. In this particular case, the transverse component of the seismograms shows zero amplitude and the  $P$ -to- $S$  wave generated is the largest (Cassidy 1992; Bertrand & Deschamps 2000). For simplicity, we only model the  $P$ -to- $S$  converted phase and we do not consider other reverberations. The resulting traces are represented Fig. 13.

As observed with the plane layer, the dipping boundary appears clearly on the time section. We present two east–west cross-sections through the power grid in Fig. 13. In the first case, direct migration is computed, whereas, in the second one, we use Snell's law to obtain a better focusing of the layer boundary by removing the ellipse smile effect. In this later migration the geometry and the depth of the discontinuity beneath the profile is accurately recovered.

## 4 RESULTS

### 4.1 Southern French Alps

From the receiver functions computed for the TGRS seismic stations we generate a grid of scattered power  $S(x, y, z)$ . The grid nodes are spaced 5 km horizontally and vertically. They define a

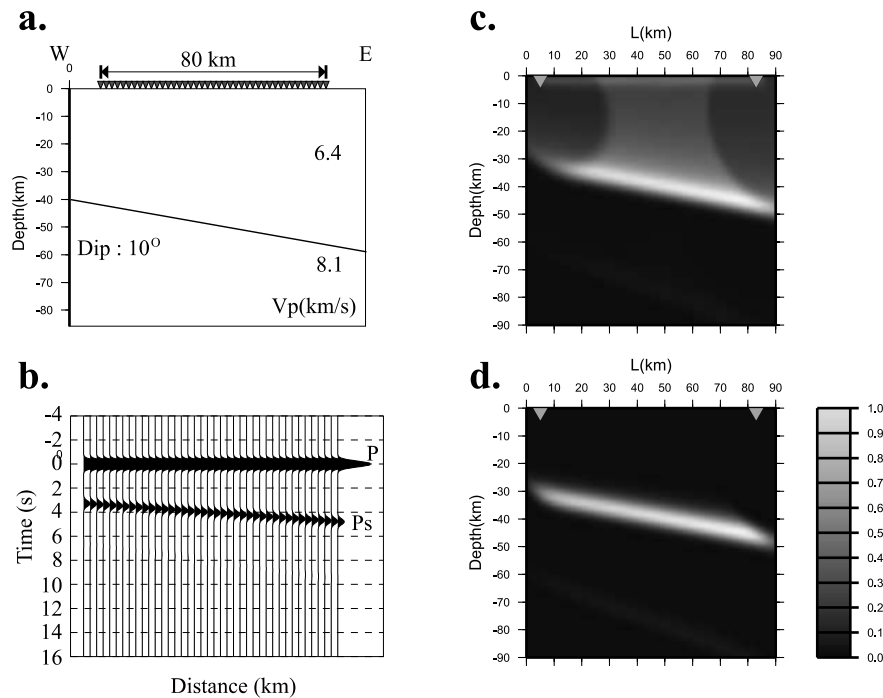


**Figure 13.** (a) Same acquisition system than for Fig. 12 but the discontinuity beneath the seismic profile is eastward dipping with an angle of  $10^\circ$ . On the receiver functions, we only model the converted  $P$ -to- $S$  phase. The dipping interface is clearly seen on the receiver function section but the true geometry is not constrained. (b) same as in Fig. 12(b). Grey triangles indicate the extension of the seismic profile.

box  $220 \times 220$  km in horizontal dimension extending from the surface to 90 km depth. Fig. 14 presents four cross-sections showing vertical slices through the volume of estimated scattering power. In these sections, good coherence is drawn in red, whereas poor coherence is indicated in purple. In this case the stations are too distant with respect to the heterogeneities of the crust and it is difficult to interpret the results in term of scatterers or lateral heterogeneity. Because of the lack of wave likelihood between the three stations even at low frequencies, the coherence maximum is typically located directly below the stations and thus should be linked to sharp velocity discontinuity. Looking at cross-section (DD') we can conclude that the main discontinuity is shallower beneath CALF than the STET station. Furthermore, with the simultaneous use of the three station receiver functions, we do not image the structure beneath SAOF. This feature could be characteristic of the crustal complexity under this station.

In order to better image the crustal structure beneath the station, we run the grid inversion for each station separately. The results we obtained are presented in Figs 15(a), (c) and (e). We plot vertical west–east cross-sections passing through each station. Because the  $P$ -wave incidence angles are in a range smaller than  $10^\circ$  and despite the number of functions stacked, the  $P$ -to- $S$  isochrones are clearly visible in the diffraction domain. At SAOF, the section underlines the high degree of lateral crustal scattering and the main signal is seen to be deeper beneath STET than CALF. At this latter station there seem to be many crustal heterogeneities very close to the recording site within a 3–4 km wide area. These heterogeneities may be related to the Castellane frontal fold-and-thrust belt. Indeed, the station is located on an east–west thrust unit (the Calern unit) which belongs to the frontal Alpine range. This unit is composed of a 2 km thick Mesozoic sedimentary cover strongly separated from the basement by a major Triassic decollement level (Laurent 1998; Masson *et al.*

1999). At STET, two distinctive parts of the diagram present high amplitudes. The first one at a depth close to 30 km can be related to the Moho. The second one looks like a scatterer near the surface 11 km east of the station.

For the identification of major plane discontinuities in the crust, we focus the energy along the ellipse using Snell's law as an *a priori* criteria (Figs 15b, d and f). We point out two main discontinuities beneath CALF. The shallower one is at 14 km depth, whereas the second, interpreted as the Moho, reaches 21 km. On the STET power map the Moho appears almost 10 km deeper, close to 30 km depth. With SAOF receiver functions the power map contains many maxima. In this case we are not able to determine the Moho depth. For the station STET we further explore the shallow scatterer that we observe on the power grid by computing synthetical receiver functions. The technique used to model the observed functions is rather simple. We use a ray tracing in a homogenous half-space in which we add a scatterer at coordinates (3, 11, 4) (N, E, Z), with the station placed at the origin of the reference frame. The traces that we obtain are plotted in Fig. 16. In this figure the synthetics compared with the real receiver functions match a phase that appears just before the Moho  $Ps$ -converted phase when the  $P$ -wave backazimuth is between  $0^\circ$  and  $90^\circ$ . For the backazimuth between  $245^\circ$  and  $300^\circ$  this phase is coincident with the Moho  $Ps$  arrival. We apply the grid power inversion to the synthetics and compare the result with that obtained for STET in Fig. 17. In the same figure, we plot a 5 km depth horizontal section through the grid. The grid deduced from the synthetics is similar to that observed for the STET station, except for the Moho discontinuity that was not considered for the synthetical computation. Finally, the horizontal section shows that the location of the scatterer is coincident with a major shear zone in the Argentera massif formed by the Valetta shear zone (VSZ) and the Bersezio fault (BF) (Malarodda *et al.* 1970; Bogdanoff 1986).

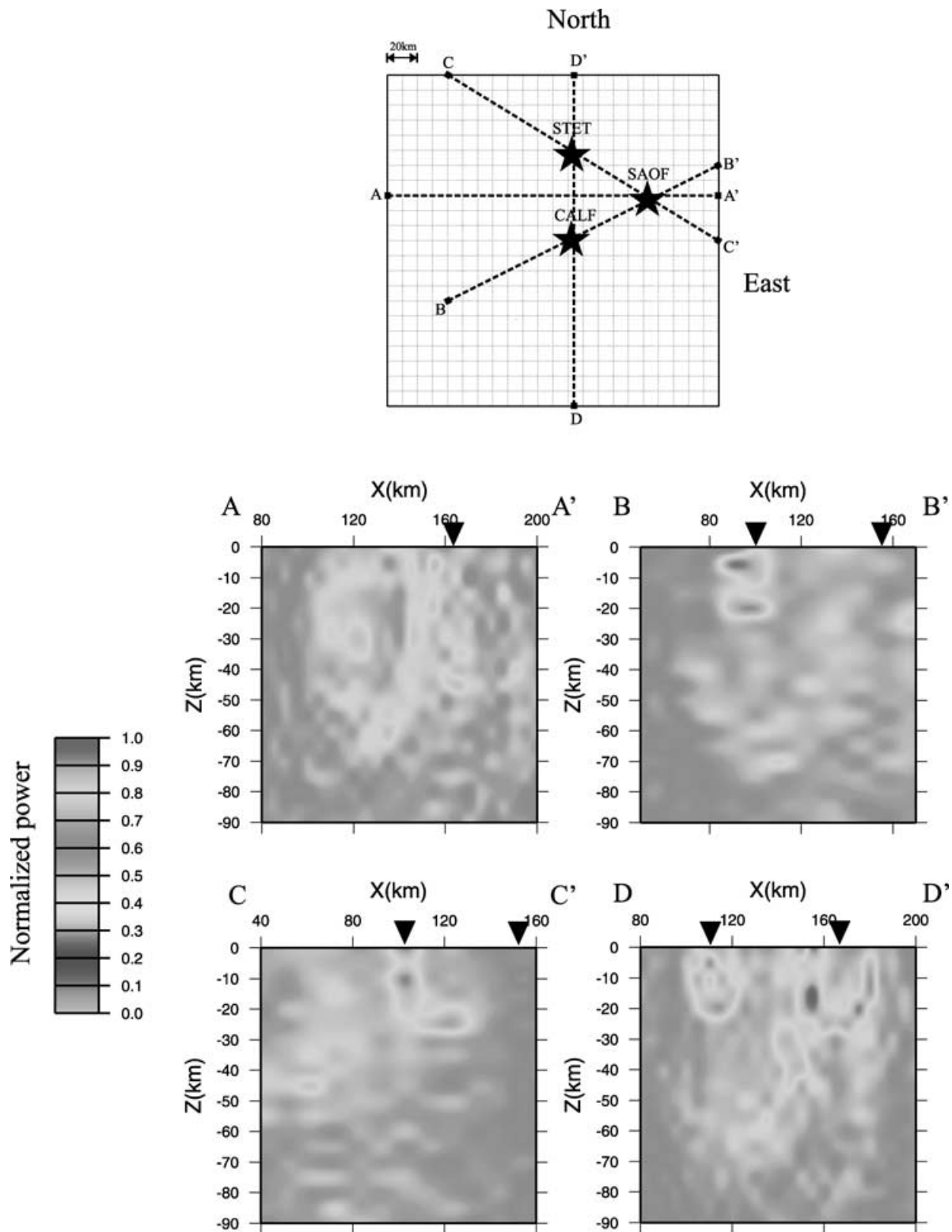
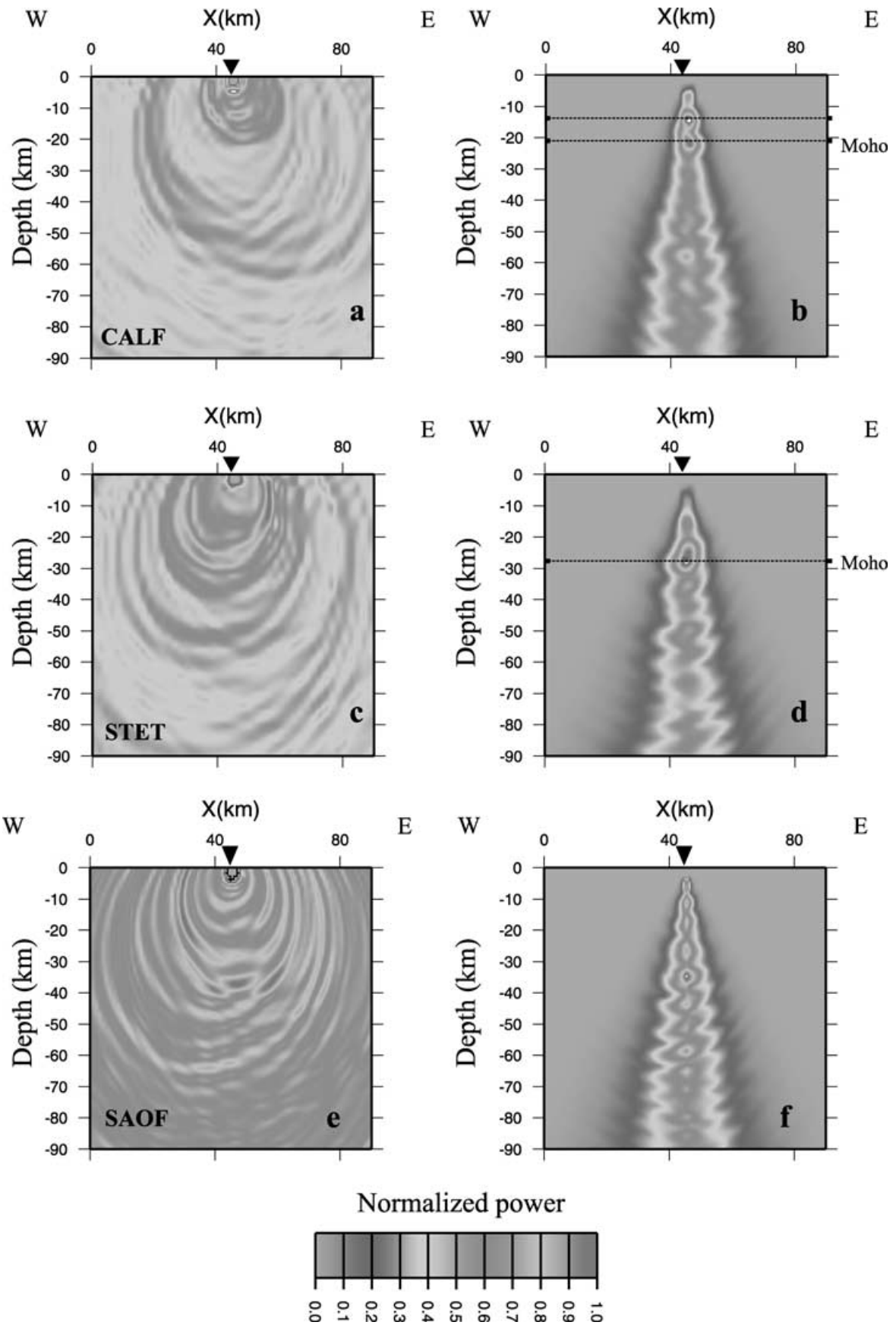


Figure 14. Vertical cross-sections through the power grid computed from the receiver functions obtained at the TGRS stations. Four different sections are used, their locations are indicated on the top of the figure.

#### 4.2 Campanian plain

A previous receiver function study (Bertrand 2000) using a semi-linearized inversion scheme (Ammon *et al.* 1990) found a SW–NE-dipping Moho in the Campanian region. For a better assessment,

we examine the data from three temporary broad-band stations installed during the BROADVES experiment near Mount Vesuvius. These stations form a southwest–northeast profile and are 25 km apart (Fig. 18). We use receiver functions computed simultaneously at the three stations (CAP, FAI and TOR) to compute the power



Downloaded from https://academic.oup.com/gji/article/150/2/524/605419 by guest on 27 January 2021

**Figure 15.** Individual power grid obtained for each station of the TGRS network. The results are plotted on E–W sections. On the right, we use Snell’s law improvement to better focus the diffracted energy along the *PS* isochrone, which is based on an interface assumption.

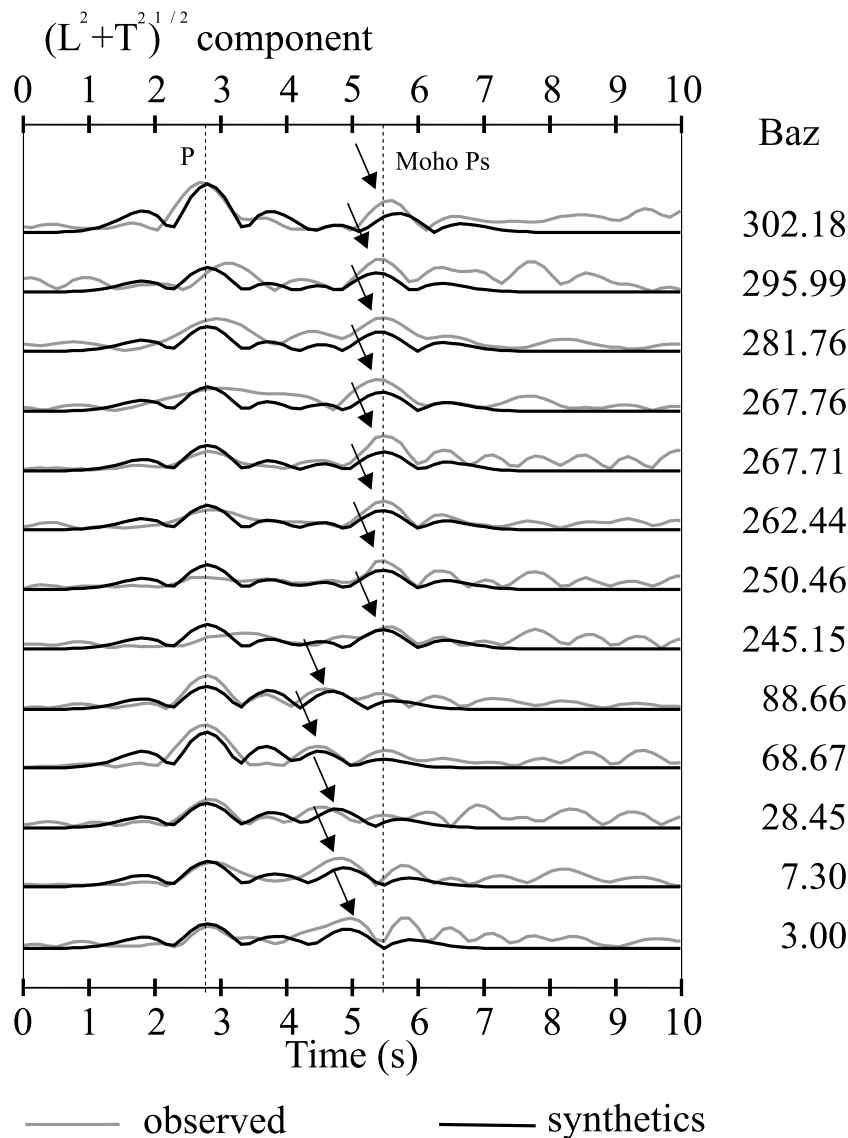


**Figure 16.** STET receiver function modelling. Backazimuth of the  $P$  wave is written on the right of the traces. The observed function are plotted over the corresponding synthetic computed for a homogeneous half-space containing a diffracting point at coordinates (3, 11, 4). The arrow indicates the arrival of the scattered phase.

grid. In order to focus the energy along the  $P$ -to- $S$  isochrones and to seek plane discontinuities beneath the seismic profile, we apply Snell's law *a priori* information. A vertical cross-section of the power grid is drawn along the profile. The power grid, normalized to a maximum value of unity, is computed within a  $100 \times 100$  km box extending to 60 km in depth. On the resulting map we detect three strong signals that can be interpreted as main discontinuities beneath the profile. Furthermore, these discontinuities are dipping northeastward (Fig. 18).

The section shows a peri-Tyrrhenian thin crust extending inland for about 33 km beneath station TOR. Beneath Capri island we show a Moho depth of almost 15 km. The deepest discontinuity is found at 35 km depth beneath CAP station, whereas its depth reaches 53 km beneath TOR station. The thin crust beneath the Campanian area is directly related to the stretching of the crust that followed the opening of the Tyrrhenian sea. This stretching resulted in an uplift of the mantle in the centre of the Tyrrhenian basin where the crust is now 5–10 km thick. The depth of the crust–mantle boundary

increases toward the Apennine chain. This main feature is clearly shown on the Bouguer gravity map (Scandone *et al.* 1991).

Furthermore, the results we present here are in good agreement with previous studies that depict the Moho doubling underneath western Italy (Scarascia *et al.* 1994). The origin of the deepest Moho could be explained in two ways. Scarascia *et al.* (1994) link this crust–mantle boundary to the southwestward subducting Adriatic plate. Because we underline a northeastward dipping direction rather than a southwestward direction, we interpret the deepest Moho as being a fossilized crust emplaced by the mid-Cretaceous subduction of the European continental margin under the oceanic segment of the Adriatic plate existing before the opening of the Ligurian and Tyrrhenian seas (Malavieille *et al.* 1998).

## 5 DISCUSSION AND CONCLUSIONS

Often in receiver function studies interpretations of fine structure are formulated in terms of layered structure (e.g. Ammon *et al.*

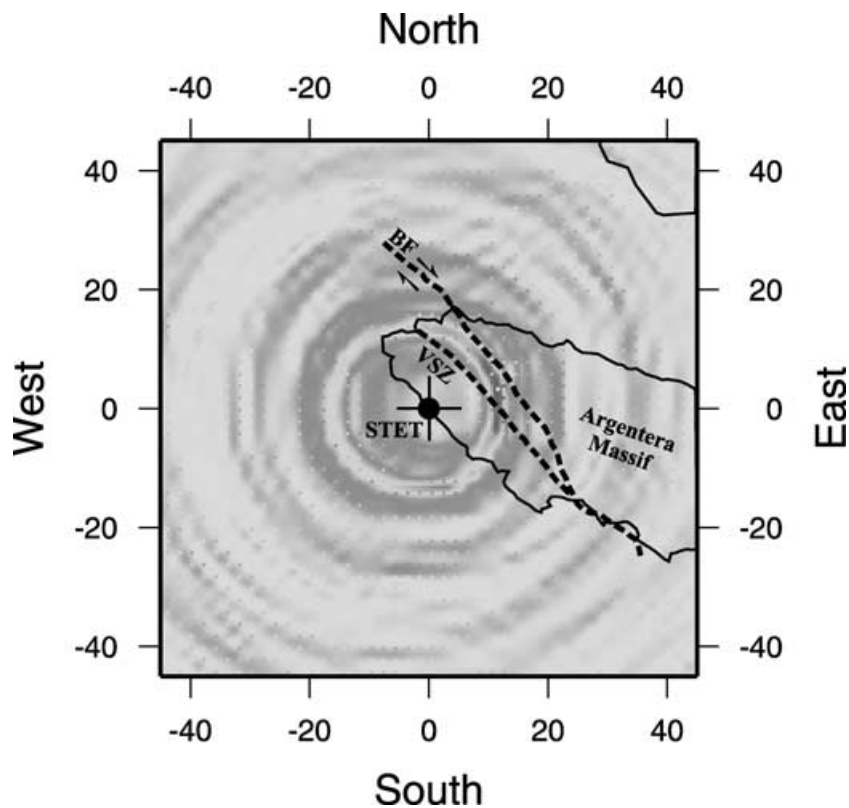


**Figure 17.** Comparison between the power map computed at STET and that obtain with the synthetical receiver functions presented in the previous figure. Horizontal section at 5 km depth in the power map computed at STET. Major tectonic features are drawn in black. BF = Bersezio fault, VSZ = Valettea shear zone. Possible near-surface scattering is observed.

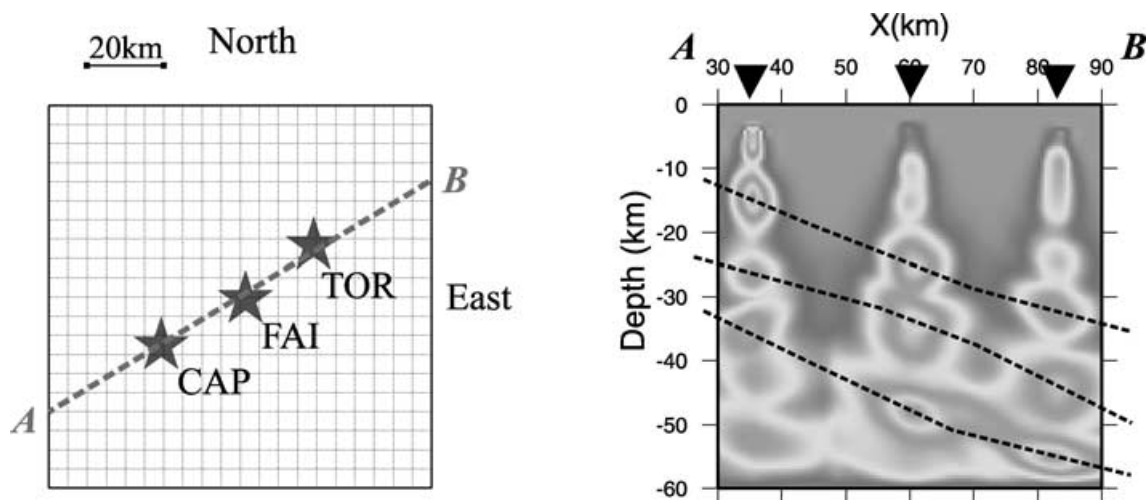


**Figure 18.** Result obtained with the receiver function of the Campanian profile (CAP, FAI and TOR, left-hand panel). A vertical section of the power grid (right-hand panel) shows energy focusing using the Snell's *a priori* information. Three dashed lines give the major dipping discontinuities observed on the section.

1990; Sandvol *et al.* 1998) and are controlled by signals at frequencies close to 1 Hz (Abers 1998). While such an approach may be valid for regions where the lateral heterogeneity is minor, in most interesting places this is not the case and signals produced by lateral scattering may be significant. Bostock (1999) proposed to use the complete reflection/transmission wavefield. We follow the same idea as, in both studied regions, lateral heterogeneity in the crust may be particularly strong as the settings are adjacent to continental collision and crustal thinning.

More and more experiments are using seismic arrays to investigate lateral heterogeneities in the crust. The aperture of the array dictates the investigation scale directly. In the present study, the seismological stations are too distant to allow an array analysis at a crustal scale. Instead, we choose to consider each station individually. With the use of 33 receiver functions, this procedure is able to relocate accurately the main discontinuities and, in particular, the crust–mantle boundary. In the case of the TGRS station STET, the dominant signal arises from a near-receiver scatterer that is probably

associated with a major shear zone. Because of their close arrival time, the signal from this scatterer could interfere with that produced by the Moho *P*-to-*S* conversion. Thus, we have to be careful when interpreting the receiver functions in terms of the horizontal plane layer. At the SAOF station, the crustal structure exhibits much more complexity. In this particular case, the use of recordings at this single station does not allow the recovery of the main crustal features. A small aperture array in the vicinity of the permanent station should provide more accurate information concerning the lateral heterogeneity of the crust in the region. The TGRS network with an aperture of 50 km is appropriate for seeking mantle structures. The proposed method could be improved by taking into account: (1) lower frequencies of the signal, (2) spherical geometry of the Earth and (3) stacking of the available signal to overcome low amplitude of the *P*-to-*S* converted waves generated in the mantle.

In southeastern France we find a Moho depth that increases from the coastline to the Alpine belt. This result is in good agreement with previous studies. In particular, a combined GPS and gravimetric experiment carried out by Calais *et al.* (1993) underlined this Moho geometry. Other seismic experiments produced similar results (i.e. Recq 1973). Furthermore, the use of the complete set of available data confirm previous results that we obtained with only part of the data (Bertrand 2000; Bertrand & Deschamps 2000). Indeed, the semi-linearized inversion (Ammon *et al.* 1990) from receiver functions computed with recordings of events coming from the north leads to the same Moho depth.

The seismic profile in the Campanian plain is well adapted to the location of the events that we recorded. Indeed, major earthquakes occur almost in the direction of the profile. Furthermore, this acquisition geometry is adequate to image discontinuities beneath the studied area. Thus we can image accurately the SW–NE dip of the crust–mantle discontinuity.

This present paper illustrates the single-scattering migration considering a homogenous crust for which the *P*-to-*S* isochrone forms an ellipse. Further improvement will concern the use of a continuously varying medium in which the scattered part of the signal is analysed, as well as a necessarily dramatic increase of broad-band seismic stations for coherent stacking and for better horizontal resolution. Furthermore, because our procedure is not able to separate the different source of scattered energy in the *P*-coda, we do not investigate multiscattering or *P*-to-*P* scattering.

## ACKNOWLEDGMENTS

We thank the TGRS staff who provided seismological data from SAOF, STET and CALF and helped us to maintain temporary stations in the regions under study. The work was funded by the GeoFrance 3-D programme. We are grateful to anonymous reviewers who helped to improve the quality of the presentation of this work. Contribution Géosciences Azur no 416.

## REFERENCES

- Abers, G.A., 1998. Array measurements of phases used in receiver-function calculations: importance of scattering, *Bull. seism. Soc. Am.*, **88**, 313–318.
- Ammon, C.J., 1991. The isolation of receiver effects from teleseismic *P* waveforms, *Bull. seism. Soc. Am.*, **81**, 2504–2510.
- Ammon, C.J., Randall, G.E. & Zandt, G., 1990. On the nonuniqueness of receiver function inversion, *J. geophys. Res.*, **95**, 15 303–15 318.
- Augliera, P., Bethoux, N., Deverchère, J. & Eva, C., 1994. The Ligurian sea: new seismotectonic evidence, *Bol. Geofis. Teor. Appl.*, **XXXVI**, 363–380.
- Bertrand, E., 2000. Sismologie large-bande: des ondes de volume aux structures de la croûte et du manteau supérieur: applications aux Alpes Maritimes et à la Campanie (Italie), *PhD thesis*, Université Joseph Fourier, Grenoble I, France, p. 302.
- Bertrand, E. & Deschamps, A., 2000. Lithospheric structure of the southern French Alps inferred from broadband analysis, *Phys. Earth planet. Inter.*, **122**, 1–2, 79–102.
- Bethoux, N., Petit, F., Rehault, J.P., Massinon, B. & Montagner, J.P., 1986. Several location methods for underwater shots in the Gulf of Genova (western Mediterranean): structural implications, *Tectonophysics*, **128**, 357–379.
- Bethoux, N., Frechet, J., Guyoton, F., Thouvenot, F., Cattaneo, M., Eva, C., Nicolas, M. & Granet, M., 1992. A closing Ligurian Sea?, *Pageoph.*, **139**, 179–194.
- Blundell, D., Freeman, R. & Mueller, St., 1992. *A Continent Revealed: the European Geotraverse*, Cambridge University Press, Cambridge.
- Bogdanoff, S., 1986. Evolution de la partie occidentale du massif cristallin externe de l'Argentera. Place dans l'arc alpin, *Géol. France*, **4**, 433–453.
- Bostock, N.G., 1999. Seismic waves converted from velocity gradient anomalies in the Earth's upper mantle, *Geophys. J. Int.*, **138**, 747–756.
- Burdick, L.J. & Langston, C.J., 1977. Modeling crustal structure through the use of converted phases in teleseismic body-wave forms, *Bull. seism. Soc. Am.*, **67**, 677–691.
- Calais, E., Carrier, A. & Buffet, G., 1993. Comparaison de données de nivellement et de positionnement par Global Positioning System: application à la détermination du géoïde dans les Alpes-Maritimes, *Compt. Rend. Acad. Sci. Paris*, **317**, 1493–1500.
- Cassidy, J.F., 1992. Numerical experiments in broadband receiver function analysis, *Bull. seism. Soc. Am.*, **82**, 1453–1474.
- Fontaine, C., 1996. Sismicité et structure en vitesse de la bordure côtière de la marge Nord Ligure à partir des données de la campagne à terre et en mer SISBALIG II. Hypothèse sur la formation et l'évolution actuelle de la marge, *PhD thesis*, Université PARIS VI, France, p. 226.
- Forgues, E. & Lambaré, G., 1997. Parametrization study for acoustic and elastic ray + Born inversion, *J. Seism. Explor.*, **6**, 253–278.
- Girardin, N. & Farra, V., 1998. Azimuthal anisotropy in the upper mantle from observations of *P*-to-*S* converted phases: application to southeast Australia, *Geophys. J. Int.*, **133**, 615–629.
- Jones, C.H. & Phinney, R.A., 1998. Seismic structure of the lithosphere from teleseismic converted arrivals observed at small arrays in the southern Sierra Nevada and vicinity, California, *J. geophys. Res.*, **103**, 10 065–10 090.
- Langston, C.A., 1977. The effect of planar dipping structure on source and receiver responses for constant ray parameter, *Bull. seism. Soc. Am.*, **67**, 1029–1050.
- Langston, C.A., 1979. Structure under Mount Rainier, Washington, inferred from teleseismic body waves, *J. geophys. Res.*, **84**, 4749–4762.
- Laurent, O., 1998. Modalités de la structuration d'un prisme de front de chaîne: L'exemple de l'arc de Castellane (chaînes subalpines méridionales, France), *PhD thesis*, Université de Nice-Sophia-Anipolis, France, p. 279.
- Lynnes, C.S. & Lay, T., 1989. Inversion of *P* Coda Isotropic Scatterers at the Yucca Flat Test Site, *Bull. seism. Soc. Am.*, **79**, 790–804.
- Malarodda, R., Carraro, F., Dal Piaz, G.V., Franceschetti, B., Sturani, C. & Zanella, E., 1970. Carta geologica del Massiccio dell'Argentera alla scala 1/50000, *Mem. Soc. géol. It.*, **IX**, 557–663.
- Malavieille, J., Chemenda, A. & Larroque, C., 1998. Evolutionary model for Alpine Corsica: Mechanism for ophiolite emplacement and exhumation of high-pressure rocks, *TerraNova*, **10**, 317–322.
- Masson, F., Verdun, J., Bayer, R. & Debegliá, N., 1999. Une nouvelle carte gravimétrique des Alpes Occidentales et ses conséquences structurales et tectoniques, *Compt. Rend. Acad. Sci. Paris*, **329**, **12**, 865–871.
- Recq, M., 1973. Contribution à l'étude de la structure de la croûte terrestre dans la région de Nice, *Bol. Geofis. Teor. Appl.*, **XV**, 161–179.
- Revenaugh, J., 1995. A scattered-wave image of subduction beneath the transverse ranges, *Science*, **268**, 1888–1892.
- Sandvol, E., Seber, D., Calvert, A. & Barazangi, M., 1998. Grid search modeling of receiver functions: implications for crustal structure in

- the Middle East and North Africa, *J. geophys. Res.*, **103**, 26 899–26 917.
- Scandone, R., Bellucci, F., Lirer, L. & Rolandi, G., 1991. The structure of the Campanian Plain and the activity of the Neapolitan volcanoes (Italy), *J. Volc. Geotherm. Res.*, **48**, 1–31.
- Scarascia, S., Lozej, A. & Cassinis, R., 1994. Crustal structures of the Ligurian, Tyrrhenian and Ionian seas and adjacent onshore areas interpreted from wide-angle seismic profiles, *Bol. Geofis. Teor. Appl.*, **XXXVI**, 5–19.
- Vinnik, L.P., 1977. Detection of wave converted from *P* to *SV* in the mantle, *Phys. Earth planet. Inter.*, **15**, 39–45.
- Vinnik, L.P., Avetisjan, R.A. & Mikhailova, N.G., 1983. Heterogeneities in the mantle transition zone from observations of *P*-to-*SV* converted waves, *Phys. Earth planet. Inter.*, **33**, 149–163.
- Virieux, J. & Farra, V., 1991. Ray tracing in 3-D complex isotropic media: an analysis of the problem, *Geophysics*, **16**, 2057–2069.
- Zollo, A. *et al.*, 1996. Seismic evidence for a low-velocity zone in the upper crust beneath Mount Vesuvius, *Science*, **274**, 592–594.